Supporting Information: Measuring Membrane Permeation Rates through the Optical Visualisation of a Single Pore

Sotiria Tsochataridou,[a‡] Greg A. Mutch,[a‡] Dragos Neagu,[a] Evangelos I. Papaioannou,[a] María Luisa Sanjuán,[b] Brian Ray,[a] Rosa I. Merino,[b] Víctor M. Orera,[b] and Ian S. Metcalfe[a]*

[a] Materials, Concepts and Reaction Engineering (MatCoRE) Research Group, School of Engineering, Newcastle University, Newcastle-upon-Tyne, NE1 7RU, UK

[b] Instituto de Ciencia de Materiales de Aragón, CSIC-Universidad de Zaragoza, C/ Pedro Cerbuna 12, 50009 Zaragoza, Spain

*Email: ian.metcalfe@newcastle.ac.uk

Fabrication of single-crystal single-pore model membranes

YSZ (8 mol% Y_2O_3) single crystal tiles (dimensions: 5 mm x 5 mm x 1mm, orientation: (110)) with two polished surfaces were purchased from PI-KEM. Blind pores were laser drilled parallel to the polished surfaces of the single crystal at Laser Micromachining Limited (Fig. S1a, b). Two sizes of single pore were constructed with dimensions as shown in Fig. S1c. Due to the inherent Gaussian shape of the laser beam, the blind-pore diameter reduced with depth. Pore mouth refers to the pore diameter at the laser incident surface.

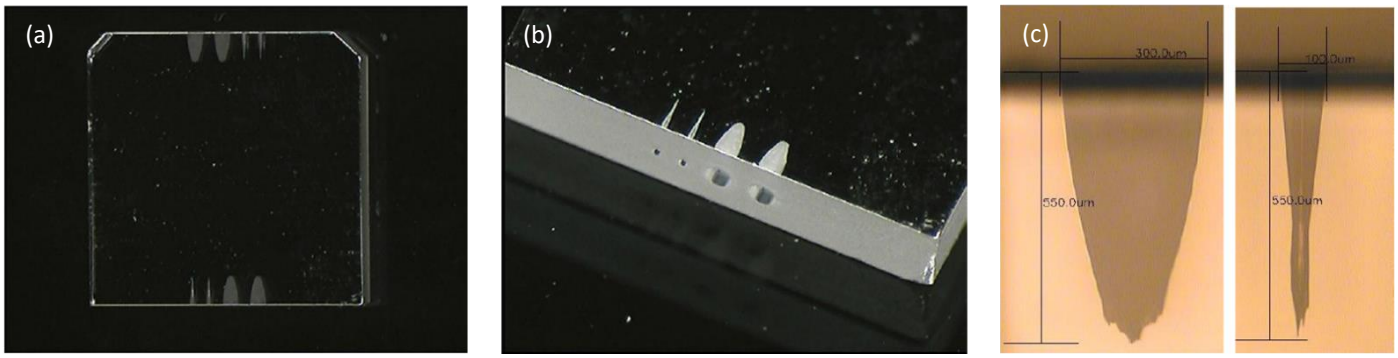

Figure. S1 Preparation of single crystal single pore model membranes. (a) YSZ single crystal tile after laser drilling. **(b)** Perspective view of the laser drilled single pores. **(c)** Dimensions of the two sizes of single pore.

Visualisation experiment procedure

A carbonate eutectic mixture (32 wt % Li_2CO_3, 33 wt % Na_2CO_3 and 35 wt % K_2CO_3) was prepared by drying the individual powders at 300 °C for 24 h, before grinding with a mortar and pestle and homogenisation in a mixing container (Fluxana, MU-K-Mixer_50Hz) with three plastic balls of 9 mm diameter for ≥ 0.5 h. A small amount (< 0.01 g) of the carbonate mixture was placed at the mouths of the laser drilled pores. The single crystal was then located in a water-cooled high temperature *in-situ* microscope stage (Linkam, TS1500). A custom-made insert was placed inside the *in-situ* cell to reduce the dead volume of the cell. The *in-situ* stage was positioned on a precision motorised platform fitted to a confocal microscope (Olympus, BX41). Video recording of the single crystal was performed through a 20x long-working-distance objective (Olympus, LMPLFLN20x). The stage was connected to two mass flow controlled gas supplies, with selection provided by a 4-way valve positioned after the mass flow controllers (Fig. S2). All flows were maintained at 50 ml min^{-1}. Gases were purchased from BOC, and comprised 50, 10, 1.1 and 0.04 mol% CO_2 in balance inert.

To infiltrate the laser-drilled pores, the single crystal was heated within the *in-situ* stage to an experimental temperature of 550 °C (a rate of 30 °C min^{-1} was used until 400 °C and then it was reduced to 1 °C min^{-1}) in a flowing 50 mol% CO_2/N_2 mixture. Upon melting, the carbonate mixture was drawn into the pores by capillary forces. Gas bubbles of varying dimensions and location were routinely present in the molten carbonate infiltrated single pores. Each of the 8 laser drilled pores was investigated, with the most clearly defined bubble selected for

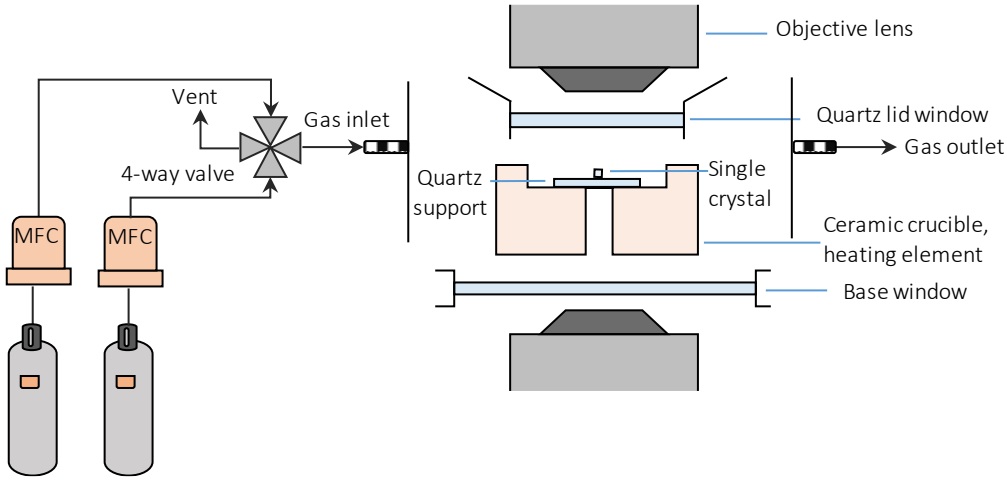

Figure. S2 Schematic of the visualisation apparatus. Mass-flow controlled gas delivery to a high-temperature *in-situ* microscope stage, hosted within an optical microscope.

experiment. It became apparent that the smaller mouth pores (*i.e.* ~100 µm Ø) provided clearer optical access to the molten carbonate, and as such were used exclusively for the experiments presented within. To begin a visualisation experiment, video recording was initiated at the conditions above (*i.e.* in flowing 50 mol% CO_2/N_2 mixture), before switching the 4-way valve to a gas flow with a lower mole fraction of CO_2. Video recording and subsequent manual or computational analysis of bubbles provided the reduction in bubble volume as it equilibrated with the changing pCO_2 in the external gas phase. Three shrinkage experiments were conducted, all initially under 50 mol% CO_2, with a switch to either to 10, 1.1 or 0.04 mol% CO_2 (*i.e.* shrinkage), and three of the reverse experiment (*i.e.* growth).

Bubble growth and shrinkage measurements

The variation of the bubble volume was calculated in two ways: manual and computational. For both methods, the videos were segmented in individual frames (~3.9 frames per second of video recording, see below Fig. S3a) and the scale of the images were determined from microscopy (Fig. S1c). For the manual measurements, individual frames were then selected and the dimensions of the bubble were measured based on a capsule-like geometry, which essentially consists of a frustum of a cone (to account for the conical shape of the pore) and two semi-ellipsoids (to account for the meniscus curves) as shown in Fig. S3b. For the computational method, the frames were further processed and analysed with Mathematica™. The frames were cropped and rotated to align the bubble vertically in order to facilitate tracking of the coordinates of parts of the bubble as highlighted in Fig. 3c. The tracking was carried out based on a custom-made algorithm using local adaptive pixel contrast. After several approaches, the method that was found to best and most reliably describe the variation of bubble volume with time for the computational method was the variation of the height of the bubble with time, as highlighted in Fig. S3c and d.

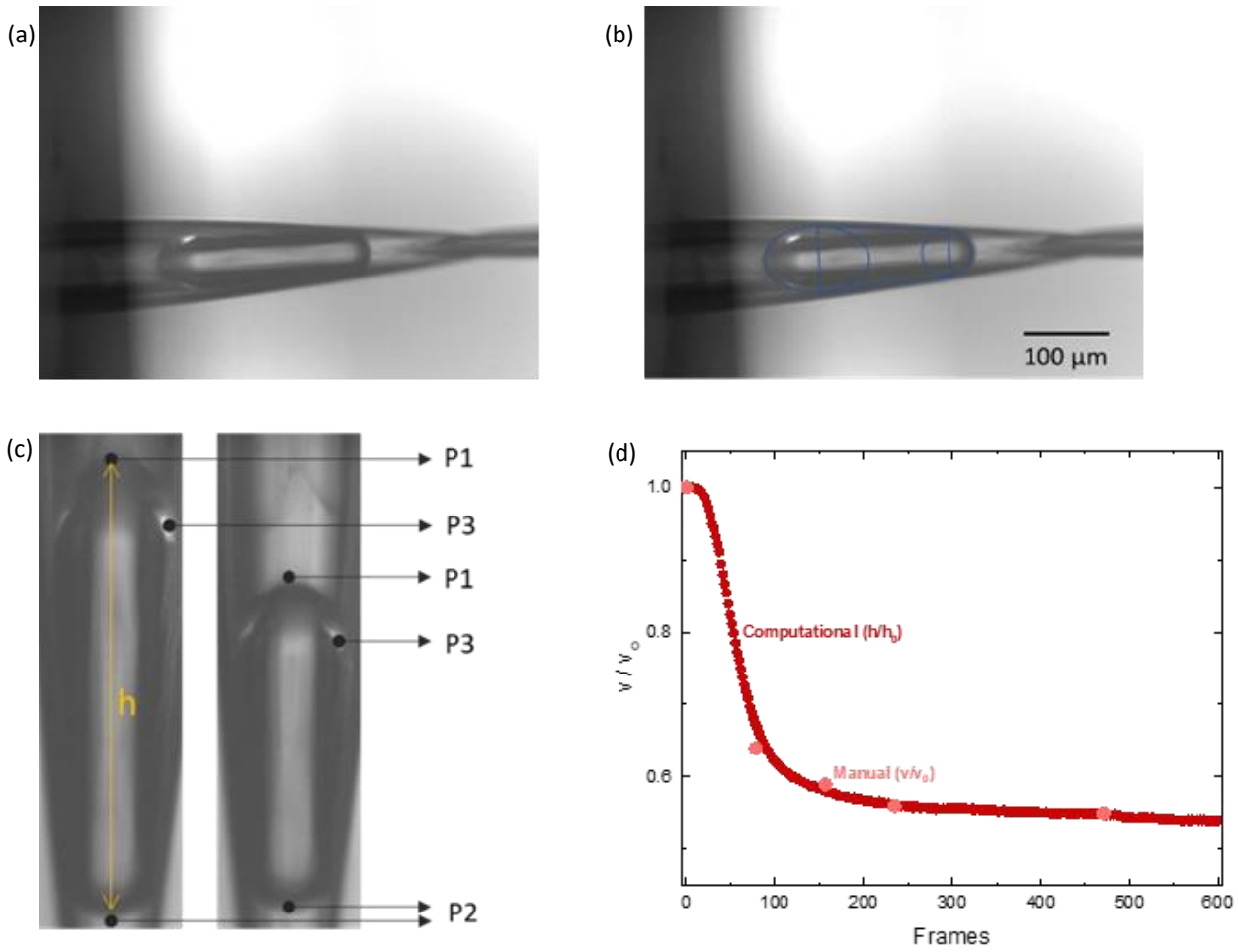

Figure. S3 Computational and manual analysis of bubble volume. (a) The first frame of an original, unprocessed video. **(b)** The frame shown in (a) annotated with a scale bar and a capsule-like construct used to model the geometry of the bubble for manual volume determination. **(c)** Cropped and rotated details from the first and last frames of a video, aligning the bubble vertically to facilitate tracking of the highlighted points using local adaptive pixel contrast (using a custom-made code in Mathematica™). **(d)** Comparison between the manual and computational results plotted as bubble volume variation normalised to starting volume (V/V_o) as a function of frame number.

Extraction of permeation rates from bubble volume changes and flux determination at low driving forces

To maintain a bubble within a liquid, there must be a pressure difference across the bubble gas-liquid interface (Fig. S4). The pressure inside the bubble may be calculated:

$$p = \frac{2\gamma}{R}$$ **Eq. S1**

Where,

p, is the overpressure within the bubble

γ, is the molten carbonate surface tension

R, is the bubble radius

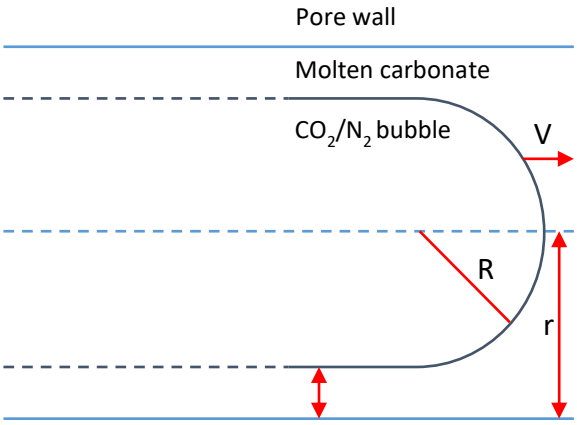

Figure. S4 Translating bubble within molten carbonate confined to the single pore model membrane. Bubble overpressure can be calculated, as well as an additional dynamic pressure that arises due to translation using Eq. S1 – S3.

In our case, the overpressure was calculated by considering a representative bubble radius (50 µm, suitable considering the single pore dimension (100 µm pore mouth radius) and position of the bubble within the single pore (routinely found roughly half way down the conical pore) and by using the molten carbonate surface tension, 235 mJ m^{-2} at 550 °C.[1] Thus, the pressure inside the bubble was ~10^4 Pa (9.4 x 10^3 Pa) above atmospheric pressure.

When a bubble confined within a liquid-filled capillary translates, if the liquid is suitably wetting on the capillary walls, a uniform thin film of liquid can separate the bubble from the wall of the confining material (Fig. S4). As the surface tension of molten carbonate 235 mJ m^{-2} at 550 °C,[1] is three orders of magnitude lower than the surface energy of the YSZ single-crystal support (1.53 J m^{-2} at 650 °C for 8 mol% Y_2O_3),[2] molten carbonate can be considered highly-wetting on YSZ.[3] As such, there is unlikely to be a contact line, with a near-zero contact angle and significant spreading. Therefore, in the present case, there is likely to be a thin film of liquid acting as a lubricant during translation, here occurring with growth or shrinkage. Due to such translation, an additional pressure develops, which can be calculated as follows.

First, a capillary number must be calculated:

$$Ca = \frac{\mu V}{\gamma}$$ **Eq. S2**

Where,

Ca, is the capillary number

μ, is the viscosity of the molten carbonate

V, is the velocity of the bubble translating within the molten carbonate

γ, is the molten carbonate surface tension

The capillary number was calculated using the viscosity of the ternary eutectic molten carbonate, 14 mPa s at 550 °C,[4] a representative bubble velocity of 8.3 x 10^{-7} m s^{-1} (here assuming a 100 µm translation in 120 s, reasonable considering the experimental results), and the molten carbonate surface tension, 235 mJ m^{-2} at 550 °C.[1] The capillary number was ~10^{-8} (4.9 x 10^{-8}).

Bretherton showed that a “dynamic pressure” can be calculated, which is the additional pressure difference across the front of the bubble due to the motion of the bubble:[5]

$$\Delta p = 3.58 \frac{\gamma}{r} (3Ca)^{2/3}$$ **Eq. S3**

Where,

Δp, is the dynamic pressure

γ, is the molten carbonate surface tension

r, is the radius of the single pore

Ca, is the capillary number

The dynamic pressure was calculated using the molten carbonate surface tension, 235 mJ m^{-2} at 550 °C,[1] a representative bubble radius (50 μm) and the previously determined capillary number. The dynamic pressure was ~10^3 Pa (4.7 x 10^3 Pa).

Thus, the total overpressure inside the bubble during translation could reach a maximum of ~10^4 Pa, by summing the bubble pressure and the dynamic pressure, representing some 10% above atmospheric pressure.

If we further assume that permeation is selective to CO_2 (considering the near perfect selectivity for CO_2 over N_2 (>1000) in molten carbonate membranes),[6] and pCO_2 inside the gas bubble at t_0 is equal to the pCO_2 of the known gas at equilibrium (the 50 mol% CO_2/N_2 mixture used during infiltration), the gas bubble volume can be used to calculate CO_2 mole fraction at any time due to pCO_2 changes to the external gas phase. If N_2 is the balance gas and its mole fraction does not change with time, then:

$$n_t = n_{CO_2,t} + n_{N_2,t} \text{ or } n_t = n_{CO_2,t} + n_{N_2,t_0} \quad \textbf{Eq. S4}$$

Where,

n_t, is the total number of moles of the gas mixture in the gas bubble at time t

$n_{CO_2,t}$ and $n_{N_2,t}$ is the number of CO_2 and N_2 moles in the gas bubble respectively at time t

n_{N_2,t_0} is the initial number of N_2 moles in the gas bubble, before changes were introduced to the external gas phase, at time t_0 (time the gas switch was made on the external gas phase)

And from the ideal gas equation, Eq. S4 will give:

$$P_t V_t = P_{CO_2,t} V_t + P_{N_2,t_0} V_{t_0} \quad \textbf{Eq. S5}$$

Where,

P_t, it the total pressure in the gas bubble at time t (the total pressure of the gas mixture in the internal gas phase is assumed to be 1 atm)

$P_{CO_2,t}$, is the CO_2 partial pressure in the gas bubble at time t

V_{t_0}, is the volume of the gas bubble at time t_0

P_{N_2,t_0} is the partial pressure of N_2 in the gas bubble at time t_0

If Eq. S5 is rearranged to make $P_{CO_2,t}$ the subject:

$$P_{CO_2,t} = P_t - \frac{P_{N_2,t_0} \cdot V_{t_0}}{V_t} \quad \textbf{Eq. S6}$$

The thermodynamic limit for the V_t/V_{t_0}, after introducing a change on pCO_2 (balance is N_2) in the external gas phase, was found from Eq. S6 and by substituting $(P_t - P_{CO_2,t})$ with $P_{N_2,t}$:

$$V_t/V_{t_0} = \frac{P_{N_2,t_0}}{P_{N_2,t}} \quad \textbf{Eq. S7}$$

For all experiments performed, the volume ratio, V_t/V_{t_0}, at the end of each experiment (t >45 min) converged with the theoretical thermodynamic limits, which indicated that the volume change of the gas bubble was a result of selective CO_2 permeation.

The permeation rate was calculated using Eq. S8:

$$Permeation\ rate = \frac{P_t \cdot |V_{t_2} - V_{t_1}|}{RT(t_2 - t_1)} \quad \textbf{Eq. S8}$$

Where,

V_{t_1}, V_{t_2} is the volume of the gas bubble at times t_1 and t_2 respectively. Fluxes were calculated by dividing permeation rates with the membrane permeation area, which was assumed to be the surface area of the mouth of the single pore, essentially the carbonate area exposed to the external gas phase (~7.9x 10^{-9} m^2).

The uncertainty in the determination of gas bubble volume is expected to be up to 1% as found from manual fitting repeats and from comparisons between the manual and computational volumes. However, the effect of the gas bubble volume uncertainty to the permeation rate was found to be negligible, as the relative range in permeation rates (upper to lower error band) did not change significantly for even higher uncertainties (Fig. S5). The error bands in permeation rate, were calculated assuming that the error was consistent across the frames (*e.g.* no variations in contrast between frames), for volume differences equal to $V_{t_2}(1 + x) - V_{t_1}(1 + x)$, where x= 0.01 or 0.20 for the upper error band and -0.01 or -0.20 for the lower error band respectively.

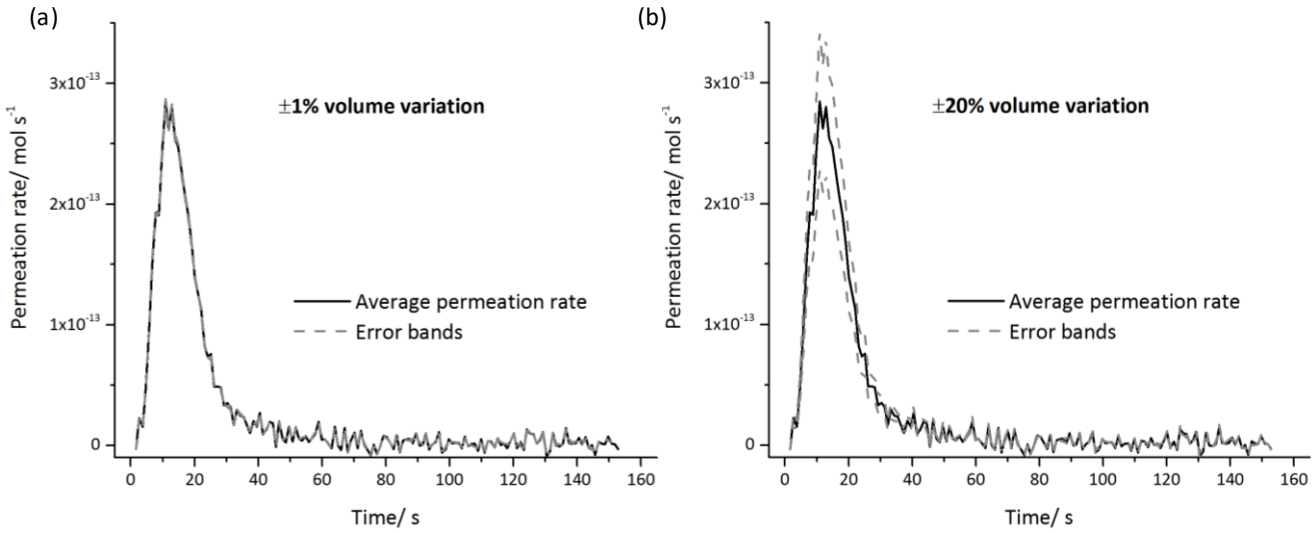

Figure. S5 Permeation rate bubble volume sensitivity analysis. Permeation rates versus time for **(a)** ±1% and, **(b)** ±20% variation of the normalised bubble volume (V/V_o) calculated computationally for the first 150 s of bubble shrinkage at 550 °C. Permeation rates were calculated using Eq. S8 and the error bands were calculated for volume differences equal to $V_{t_2}(1+x) - V_{t_1}(1+x)$, where **(a)** x= 0.01 for the upper band and -0.01 for the lower error band and, **(b)** x= 0.20 for the upper band and -0.20 for the lower error band.

Supplemental permeation rate extraction from bubble volume changes

Fig. 2 in the main manuscript provides normalised volume and permeation rate variation, as well as permeation rates for a visual permeation experiment utilising gas composition switches between 10 and 50 mol% CO_2. Below, is an identical experiment but for composition switches between 1.1 and 50 mol% CO_2.

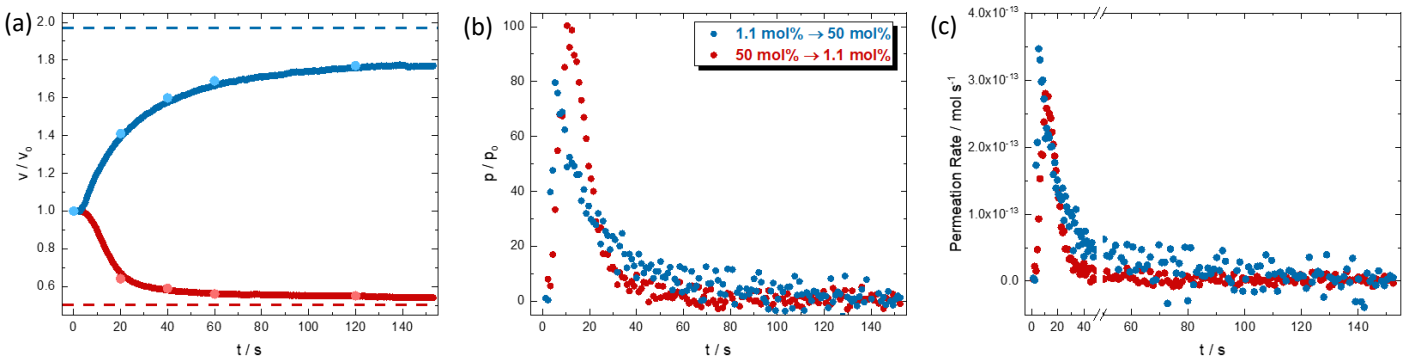

Figure. S6 Extraction of permeation rates from bubble volume changes. (a) Normalised bubble volume variation calculated using manual image measurement at t = 0, 20, 40, 60 and 120 s, with the computational measurement shown as a darker shade and with a temporal resolution of 0.255 s. **(b)** Normalised permeation rate. **(c)** CO_2 permeation rates extracted from growth (blue) and shrinkage (red) of CO_2/N_2 bubbles. During the initial ~30 s, the permeation rate increased then decreased, as equilibrium with the external environment was approached. Subsequently, permeation rate remained low as the driving force for permeation was low.

Multiple-pore membrane preparation

YSZ (3 mol% Y_2O_3) closed-end tubes were obtained from Precision Ceramics as a custom order. The closed-end tubes were 235 mm in length, with internal diameter of ~15 mm and external diameter of ~19 mm. The closed-end thickness was ~500 μm, confirmed by micro-CT analysis (Fig. 4c). Laser drilling of 1000 single pores was carried out at Laser Micromachining Limited to produce a multiple pore membrane (Fig. 4b).

The pores exhibited a truncated cone shape, with a diameter of ~350 μm on the laser incident surface and ~100 μm on the opposite surface. The pore diameter of 100 μm was chosen in order to equal the mouth diameter of the single-pore single crystal and was used as the permeate side of the membrane.

Multiple-pore membrane experiment procedure

The multiple pore membrane support was infiltrated with molten carbonate to form a supported molten-salt membrane. To do so, a carbonate pellet was prepared by placing the carbonate mixture described above in a 12 mm diameter stainless steel die, which was pressed at 5 tons for 1 min (Atlas™ Series Hydraulic Presses T28, Specac). The mass of the pellet was calculated so that the total volume of the multiple pores was infiltrated with molten carbonate. The carbonate pellet was placed on the drilled surface of the multiple-pore membrane and placed in a custom-made membrane reactor (Fig. 4a). The reactor comprised two chambers, the internal (permeate-side) and external (feed-side) chamber, with volumes of ~30 cm^3 and

~600 cm^3 respectively. Residence-time distribution experiments showed that the gases were well-mixed in both chambers. Therefore, the membrane was considered to be exposed to the composition measured at the outlet of the chamber. Due to the unique design of the multiple-pore membranes, a low temperature sealant (high-vacuum silicone grease) was required on the open end of the tube, in the stainless-steel base, to achieve a well-sealed membrane system with no detectable leaks (leaks were below the detectable limit of our analytical instrumentation). To begin a permeation experiment, the membrane was heated above the melting point of the carbonate mixture (~400 °C), causing the carbonates to melt and infiltrate the drilled pores, due to capillary forces. Heating was carried out at a rate of 1 °C min^{-1} in a flowing 50 mol% CO_2/N_2 mixture supplied to both the feed and permeate sides of the membrane.

To begin a permeation experiment, the 50 mol% CO_2/N_2 mixture supplied to the feed-side inlet was maintained, with Ar supplied to the permeate-side inlet, therefore establishing a driving force for CO_2 permeation. A range of feed (90, 77, 50, 25 mol% CO_2) and sweep (1.1, 0.1, 0.04 mol% CO_2 and Ar) gases were used to probe different driving forces. All experiments were conducted with 50 ml min^{-1} flows, and at 550 °C. The outlet gases of the permeate side were analysed with a CO_2 IR analyser (LI-COR, LI-840A) connected in series with a mass spectrometer for N_2 leak detection (HIDEN, HALO 100-RC). If N_2 was detected (~10 ppm limit of detection) the experiment was stopped as the membrane was leaking. The mass spectrometer was calibrated prior to the experiment using Ar and 0.04 mol% N_2/Ar. The IR analyser was calibrated using a 3-point calibration with Ar, 0.04 mol% and 1.1 mol% CO_2/Ar and has a specified measurement range of 0 – 2.0% CO_2, accuracy of <1.5% of reading, total drift at 0.037% CO_2 of <0.0004%/°C CO_2 and RMS noise <0.001% CO_2.

Calculation of permeation rates and fluxes in multiple-pore membranes

Permeation rates were calculated using the flow rate, Q, and the difference between the average mole fraction of CO_2 at steady state in the outlet stream of the permeate side ($x'_{CO_2\,(outlet)}$, where $'$ refers to the permeate side) and the mole fraction of CO_2 at steady state in the inlet stream of the permeate side ($x'_{CO_2\,(inlet)}$).

$$Permeation\ rate = \left(x'_{CO_2\,(outlet)} - x'_{CO_2\,(inlet)}\right) \cdot Q \qquad \textbf{Eq. S9}$$

Fluxes were calculated by dividing permeation rates by the membrane permeation area, which was assumed to be the surface area of the pores exposed to the feed side gas.

Literature data for flux comparison with single-pore and multiple-pore membranes

To demonstrate the utility of the visualisation approach in determining CO_2 flux in supported molten-salt membranes, a representative selection of data from the literature was selected for comparison. The data was taken for membrane operation as close to 550 °C as possible (*i.e.* the temperature of our experiments), and where this was not available the data taken was for membrane operation at 600 or 650 °C. Where a range of driving forces were examined at one temperature, the flux for the lowest driving force was taken, to be conservative in our approach where we state that the single-pore membrane experiments permit exploration of a previously unexplored low driving-force region. For further detail, the reader is referred to the references in Table S1.

Table. S1 Representative literature data for supported molten-salt membranes.

Membrane Support Material	Driving Force (ln ($pCO_{2\,(feed)}$ / $pCO_{2\,(permeate)}$))	Flux (ml min^{-1} cm^{-2})	Reference
$Ce_{0.8}Sm_{0.2}O_{1.9}$ (SDC)	4.4	100	[7]
SDC/$Bi_{1.5}Y_{0.3}Sm_{0.2}O_3$ (BYS)	9.8	161	[8]
YSZ	6.8	25	[9]
CeO_2	9.3	1.8	[10]
Al_2O_3/BYS	5.0	45	[11]
SDC	4.9	350	[12]
YSZ	3.9	4.4	[13]
Stainless Steel	8.1	17	[14]
YSZ/BYS	4.1	108	[15]

Residence time distribution experiment for single-pore model membrane *in-situ* cell

To calculate a driving force (ln ($pCO_{2\,(feed)}$/$pCO_{2\,(permeate)}$) for permeation during visualisation experiments, $pCO_{2\,(feed)}$ and $pCO_{2\,(permeate)}$ must be determined. Here, a difference in pCO_2 between the external gas mixture composition (in the *in-situ* cell) and the internal gas mixture composition (in the gas bubble) will give rise to the driving force. Note that $pCO_{2\,(feed)}$ and $pCO_{2\,(permeate)}$ swap depending on whether the bubble grows or shrinks. The internal gas mixture composition can be calculated directly using the bubble volume data, such as that in Fig. 2c, and Eq. S6. The external gas mixture composition can be determined from residence time distribution experiments with the *in-situ* cell following the step-change in gas composition that causes bubble growth or shrinkage. Thus, residence time distribution experiments were conducted to determine the external pCO_2 by applying a step-change in composition, 50 to 1.1 and 0.04 mol% CO_2. The response was identical with an R^2 of 0.998 for both step-changes. Note that the response time of the analytical apparatus was found to be more than one order of magnitude faster than the *in-situ* cell and thus did not contribute significantly to the residence time.

We extract CO_2 fluxes at small driving forces 100 – 150 s after the step-change (at ~100 s in Fig. S7), as the external gas mixture composition is relatively steady and known from the residence time distribution (at ~200 – 250 s in Fig. S7). During 100 – 150 s the average normalised composition is 0.986 (ranging from 0.975 to 0.994). Therefore, for a step-change to 50% from 1.1%, one can expect the average external composition to be 49.30 mol% CO_2 (ranging from 48.75 to 49.70 mol% CO_2). A similar average and range can be calculated for the internal composition during 100 – 150 s. Therefore, an uncertainty in the driving force can be estimated by using the limits of the ranges on both external and internal to calculate a minimum and maximum possible driving force (shown as error bars on Fig. 3). It is important to note that this approach results in negative driving forces for shrinkage experiments with gas composition changes from 50 to 1.1. and 0.04 mol% CO_2 (as the average external CO_2 mol% is lower than that within the bubble, which therefore cannot result in shrinkage). This is likely due to "dead zones" in the *in-situ* cell that result from poor mixing, which is less likely to be a problem upon an increase in concentration.

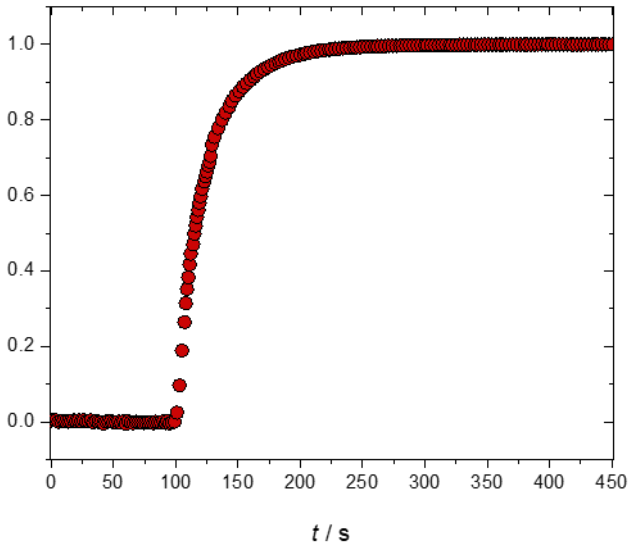

Figure. S7 Residence time distribution of *in-situ* cell. At ~100 s a gas step-change is imposed. After a further ~100 s the gas composition within the *in-situ* cell has approached steady-state. The data has been normalised using $y_{normalised} = (y_t - y_{min})/(y_{max} - y_{min})$, using measured minimum and maximum values.

References

(1) Igarashi, K.; Tajiri, K.; Asahina, T.; Kosaka, M. Surface Tension Around Eutectic Compositions of Molten Alkali Carbonate Mixtures. *Zeitschrift fur Naturforsch. A* **1992**, *47*, 675–677.

(2) Tsoga, A.; Nikolopoulos, P. Surface and Grain-Boundary Energies in Yttria-Stabilized Zirconia (YSZ-8 Mol %). *J. Mater. Sci.* **1996**, *31*, 5409–5413.

(3) Mutch, G. A.; Qu, L.; Triantafyllou, G.; Xing, W.; Fontaine, M.-L.; Metcalfe, I. S. Supported Molten-Salt Membranes for Carbon Dioxide Permeation. *J. Mater. Chem. A* **2019**, *7*, 12951–12973.

(4) Kim, S. W.; Uematsu, K.; Toda, K.; Sato, M. Viscosity Analysis of Alkali Metal Carbonate Molten Salts at High Temperature. *J. Ceram. Soc. Jpn.* **2015**, *3*, 355–358.

(5) Bretherton, B. F. P. The Motion of Long Bubbles in Tubes. *J. Fluid Mech.* **1960**, *10*, 166–188.

(6) Cerón, M. R.; Lai, L. S.; Amiri, A.; Monte, M.; Katta, S.; Kelly, J. C.; Worsley, M. A.; Merrill, M. D.; Kim, S.; Campbell, P. G. Surpassing the Conventional Limitations of CO_2 Separation Membranes with Hydroxide/Ceramic Dual-Phase Membranes. *J. Memb. Sci.* **2018**, *567*, 191–198.

(7) Tong, J.; Zhang, L.; Han, M.; Huang, K. Electrochemical Separation of CO_2 from a Simulated Flue Gas with High-Temperature Ceramic – Carbonate Membrane : New Observations. *J. Memb. Sci.* **2015**, *477*, 1–6.

(8) Lu, B.; Lin, Y. S. Asymmetric Thin Samarium Doped Cerium Oxide-Carbonate Dual-Phase Membrane for Carbon Dioxide Separation. *Ind. Eng. Chem. Res.* **2014**, *53*, 13459–13466.

(9) Zuo, M.; Zhuang, S.; Tan, X.; Meng, B.; Yang, N.; Liu, S. Ionic Conducting Ceramic-Carbonate Dual Phase Hollow Fibre Membranes for High Temperature Carbon Dioxide Separation. *J. Memb. Sci.* **2014**, *458*, 58–65.

(10) Xing, W.; Peters, T.; Fontaine, M. L.; Evans, A.; Henriksen, P. P.; Norby, T.; Bredesen, R. Steam-Promoted CO2 Flux in Dual-Phase CO_2 Separation Membranes. *J. Memb. Sci.* **2015**, *482*, 115–119.

(11) Rui, Z.; Anderson, M.; Li, Y.; Lin, Y. S. Ionic Conducting Ceramic and Carbonate Dual Phase Membranes for Carbon Dioxide Separation. *J. Memb. Sci.* **2012**, *417–418*, 174–182.

(12) Zhang, L.; Xu, N.; Li, X.; Wang, S.; Huang, K.; Harris, W. H.; Chiu, W. K. S. High CO_2 Permeation Flux Enabled by Highly Interconnected Three-Dimensional Ionic Channels in Selective CO_2 Separation Membranes. *Energy Environ. Sci.* **2012**, *5*, 8310–8317.

(13) Wade, J. L.; Lee, C.; West, A. C.; Lackner, K. S. Composite Electrolyte Membranes for High Temperature CO_2 Separation. *J. Memb. Sci.* **2011**, *369*, 20–29.

(14) Chung, S. J.; Park, J. H.; Li, D.; Ida, J. I.; Kumakiri, I.; Lin, J. Y. S. Dual-Phase Metal-Carbonate Membrane for High-Temperature Carbon Dioxide Separation. *Ind. Eng. Chem. Res.* **2005**, *44*, 7999–8006.

(15) Lu, B.; Lin, Y. S. Synthesis and Characterization of Thin Ceramic-Carbonate Dual-Phase Membranes for Carbon Dioxide Separation. *J. Memb. Sci.* **2013**, *444*, 402–411.